

THE OBTAINING OF HIGH SENSITIVITY AND SPECIFICITY TRANSDUCER MEDIA FOR SENSORS SPECIALIZED IN BIOLOGICAL TOXIN DETECTION

N. PETREA^{a*}, P. ZAMORA IORDACHE^a, V. ȘOMOGHI^a, I. SAVU^a,
M. MUREȘAN^a, R. PETRE^a, L. RECE^a, R. LUNGU^a, A. PRETORIAN^a,
G. MITRU^a, B. DIONEZIE^b, B. SAVU^c, L. MUTIHAC^d, L. KIM^d,
V. ORDEANU^e

^aScientific Research Center for NBC Defence and Ecology, 225, Olteniței, Bucharest, Romania

^bPolitehnica University of Bucharest – Biomaterials Research Center, 313, Spl. Independentei, Bucharest, Romania

^cPolitehnica University of Bucharest, Center for Microscopy- Microanalysis and Information Processing, 313 Spl. Independentei, 060042, Bucharest, Romania

^dUniversity of Bucharest, Department of Analytical Chemistry, 4-12, Regina Elisabeta Blvd., 030018 Bucharest, Romania

^eMedico-Military Scientific Research Center, 37, C.A. Rosetti, Bucharest, Romania

This paper presents the experimental results obtained as a result of the testing on castor of a new type of nanocomposite superparamagnetic material. The purpose of the biochemical fixing tests was to obtain information concerning the characteristics of the biochemical fixing: efficiency, mechanisms, etc. The tested nanocomposite structure represents a new nanocomposite material, of the $(ECH)_{n\beta}\{-Fe_3O_4-n[SiO_{1.5\gamma}-(CH_2)_3(NH_2)](NH_2)_{n\delta}\}-(GL)_{n\epsilon}$ type $[(ECH)_{n\beta}-(GL)_{n\epsilon} \rightarrow$ coated and polyvalently biochemically activated nanoparticles $\{n[SiO_{1.5\gamma}-(CH_2)_3(NH_2)](NH_2)_{n\delta} =$ coating layer; $(NH_2)_{n\delta}, -NH_2 =$ shallow layer of amino groups $(GL)_{n\epsilon} =$ shallow molecular layer of glutaraldehyde $(ECH)_{n\beta} =$ shallow molecular layer of epichlorhydrine}. In order to obtain eloquent information concerning the $-NH_2, =NH, -NH_3OH, -SH, -OH, -S-S-$ haptene distribution, the magnetite nanoparticles were synthesised through the reversed mycelia method. Another main objective was to verify the concept of dynamic and in real time 'undestructive biochemical fixing'. The veridicity of this concept offers the possibility of applying npa-BC in thin sensitive layers, on interfaceable supports of the following types: thin oxide and metallic layers, electronic transducers, interfaces amplifying the electric signal, etc.

(Received August 17, 2009; accepted October 1, 2009)

Keywords: Biochemical sensors, Reversed mycelia, Biochemical activation, Ricin, Fe_3O_4 , Confocal microscopy

1. Introduction

Sensors represent energy converters, they are defined as devices that receive and respond to the action of a stimulus [1]. From the analytical point of view, sensors define particular cases of information transfer from the environment that responds to the stimulus (transducer medium) to the signal (information) extraction electronic interface, via the transformation and transfer function of the stimulus [1]. Mainly, the sensor's function is to specifically respond to a particular physical property (stimulus) and convert it into an electrical signal compatible with the detection electronics

* Corresponding author: nicoleta.petrea@yahoo.com

(Fig. 1). Sensors are not stand-alone entities, always being associated with complex systems that can integrate other detectors, signal conditioners, signal processors, data drives, actuators, etc.

Stimuli can be of different nature: acoustic, mechanical, biological, chemical, viscosity, electrical, radiation, thermal, magnetic, optical, etc. [2]. Depending on the nature of the stimulus, the specific transducer application is defined, or the transducer that is specific to the stimulus.

The transducers [3] represent distinct components of the sensors, performing the conversion function of a type of energy into another type of energy. In most cases, transducers are oriented applications with a high degree of specificity. The specificity is oriented by the type of stimulus, so as the signal / noise (S / N) ratio should be a useful one in terms of data acquisition. The value of the S / N ratio, the excitement intensity of the stimulus and the quality of the analytical function of processing the input and output stimulus from the transmitter, are the criteria that define the choice of the type of the transducer's sensitive medium. These causes are reflected in the transfer function of the sensor, which aims to correlate the analytical function of signal and information transfer, from the stimuli to the electronics that serves the sensor, including the transducers, etc. [1].

The real-time detection of biochemical structures (bacteria, viruses, toxins, etc.) is strongly influenced by the concentration and complexity of the macromolecular structure of the biochemical analyte. In addition to the enzyme tests, all the other biochemical detection techniques and methods involve the integration of a transducer which should convert an accessible stimulus in terms of experimental measurement, in a stimulus which is specific to the investigated biochemical structure. Because most biological structures contain natural biological aminoacids (tryptophan, tyrosine, aromatic derivatives, etc.), the most used stimuli for biochemical awareness are fluorescence inducing electromagnetic radiations. The stimuli that induce fluorescence specific to natural aminoacids present an excitation spectrum below 290nm. Often, in biochemical applications fluorescence inducing electromagnetic stimuli located in the 200÷650nm spectral range are used.

The utilization of specific fluorescence inducing electromagnetic stimuli represents a convenient way to quickly obtain a measurable electrical signal in relation to the excitation stimuli. In fact, the signal generated by the transducer represents the contribution of all fluorochroms that can be excited at the stimulus wavelength. These fluorochromes are present in the immediate vicinity of the stimulated biochemical structure's surface, and their contribution to the fluorescence spectrum is called the surface fluorescence fingerprint.

Because of the low concentration of the biochemical analytes of interest present in the monitored area, a direct stimulation of the biochemical transducer cannot be accomplished, because the transfer function cannot be accordingly discriminated in relation to the background noise. The improvement of the obtaining conditions of a reasonable transfer function of a biochemical sensor (Fig. 2), is currently carried out through the following procedures: (a) biochemical analyte concentration (b) obtaining biochemical transducers with superior transformation coefficients of the stimulus and high specificity (c) the use of advanced electronic components for amplification, conditioning and signal acquisition.

The experimental researches presented in this paper were directed towards obtaining a composite nanostructure which should provide superior biochemical fixation coefficients (effectiveness, efficiency) and which could accomplish a viable interface between the biological toxin stimulus, the detection sensor attached to the application and the signal generated by the detector (Fig. 1). To achieve this objective it is very important to obtain a transducer medium which could achieve a good compromise between the size of the fixing component and the biochemical fixation coefficients. The obtaining of an adequate balance between these factors, favors the application of transducer material directly on oxide layers and thin metal layers, semiconductor layers, doped composite layers etc.

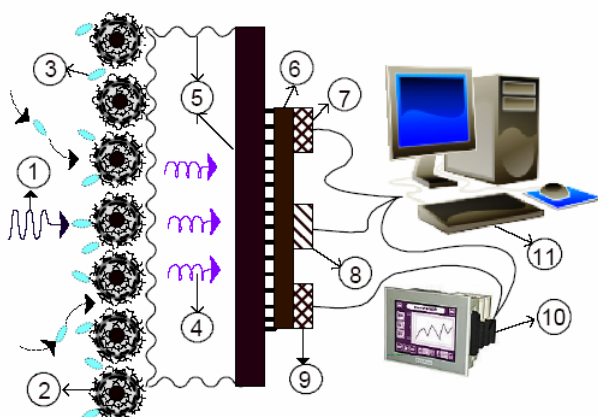


Fig.1 The theoretical chain of phenomenological processes involved in the design and construction of a biological detection sensor [1-stimulus, 2-biochemical fixation sensitive medium (biochemical transducer), 3-biochemical analyte, 4-electrical signal, 5-electronic interface, 6- electronic intermediate processing circuit of the signal, 7-I/O, 8-electrical power supply, 9- temporary synchronization port with other systems, 10-process actuators, 11-control unit]

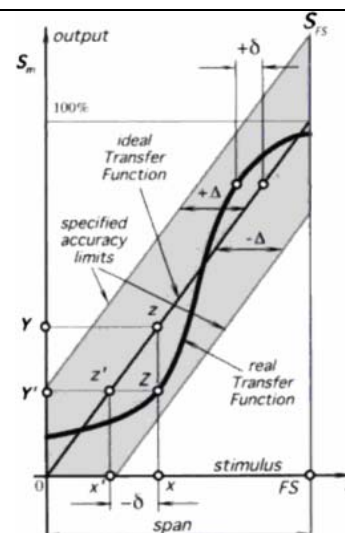


Fig.2 Schematic representation of the transfer function $S = f(s)$ of a sensor [1]:

- S = generated electrical signal at the output of the sensor
- s = stimulus

2. Experimental

2.1 The obtaining of $\text{Fe}_3\text{O}_4\text{-n}[\text{SiO}_{1.5\gamma}\text{-(CH}_2\text{)}_3\text{(NH}_2\text{)}](\text{NH}_2)_{n\delta}$ marked with rhodamine B

$\text{Fe}_3\text{O}_4\text{-n}[\text{SiO}_{1.5\gamma}\text{-(CH}_2\text{)}_3\text{(NH}_2\text{)}](\text{NH}_2)_{n\delta}$ (**np**) represents a complex polyvalent nanocomposite structure, which will be polyvalently activated with glutaraldehyde and epichlorohydrin to improve the effectiveness and efficiency of the biochemical fixing of the heterodimeric plant toxin ricin [4]. In order to carry out thorough biochemical investigations by confocal microscopy, np were marked with rhodamine B, and the castor was marked with fluoresceine isothiocyanate (FITC).

2.1.1 Synthesis of Fe_3O_4 nanoparticles using the reverse micelle method (MI)

The following solutions were prepared separately: **(RM-S1)** 200ml of distilled water, 20 grams of sodium dodecil sulphate (SDS - analytical purity, Sigma Aldrich), 70 milliliters of hexane and 10.3 grams of $\text{FeCl}_2 \cdot 4\text{H}_2\text{O}$; **(RM-S2)** 200m of water distilled, 20 SDS, 70 milliliters of hexane and 12.7 NaOH; **(SF-Rb)** 1mg of rhodamine B + 10ml of absolute ethylic alcohol [5].

The SF-Rb mixture was stirred mechanically (300rpm) for two hours. Before the initiation of the nucleation reaction of Fe_3O_4 , the RM-S1 and RM-S2 solutions were vigorously stirred in order for the SDS to become soluble and to favour the mycelium formation (Fig.3 (a), Fig.3 (b)) [6]. After reaching the optimum homogenization point, characteristic for the uniformly distributed mycelium formation, RM-S2 has been added over the RM-S1, under mechanical stirring (300rpm). The reaction was left for perfecting for six hours (300rpm, 27°C), then the obtained suspension was washed successively with: (1) 200ml of ethylic alcohol (until traces of hexane were not observable any longer) (2) 200ml nitric acid 2M (for fifteen minutes, 300rpm) [7] (3) twice with 500ml of distilled water (4) 200ml solution of trisodium citrate (12.5%) (for fifteen minutes, 300rpm) (5) twice with 500ml of distilled water. The separation of the magnetite nanoparticles after successive washing processes was done by centrifugation (Sigma - $t=5$ minutes, $v=3000\text{rpm}$).

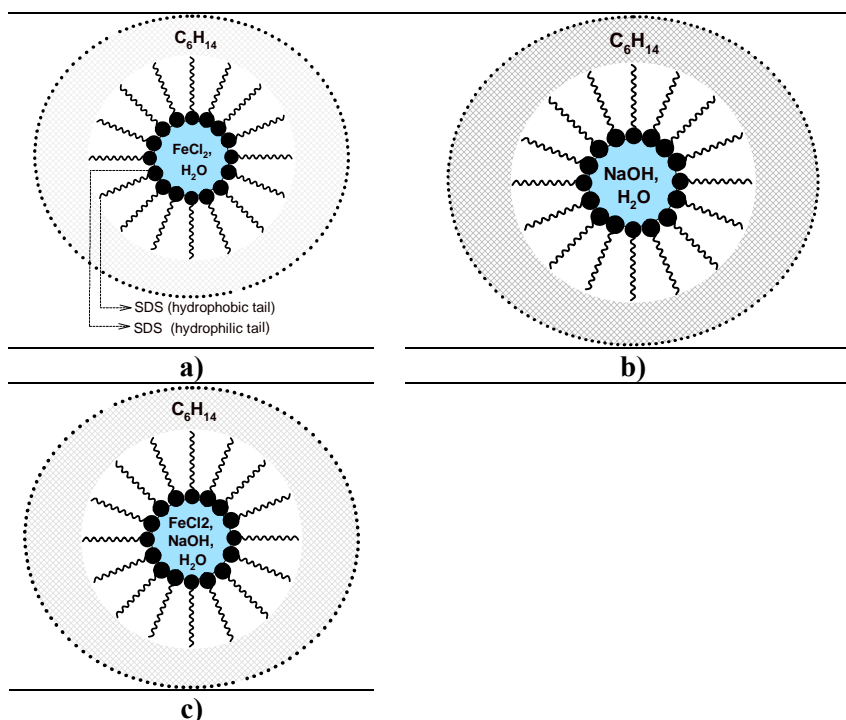


Fig.3 The aqueous and hydrophobic phase distribution in the case of *reverse micelia* method: a) distribution of aqueous and oil phases, in the case of the micelium formed in RM-S1 b) distribution of aqueous and oil phases, in the case of the micelium formed in RM-S2 c) distribution of aqueous and oil phases, formed after the RM-S1 and RM-S2 solutions came into contact.

2.1.2 $Fe_3O_4-n[SiO_{1.5\gamma}-(CH_2)_3(NH_2)](NH_2)_{n\delta}$ syntethesis marked with rhodamineB (Rb) \rightarrow the obtaining of $Fe_3O_4-n[SiO_{1.5\gamma}-(CH_2)_3(NH_2)](NH_2)_{n\delta}(Rb)_{np}$ (np-Rb)

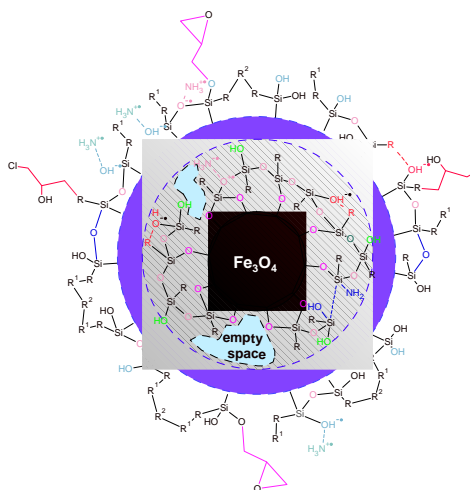


Fig.4 The chemical and topological structure of (ECH)-npa-(GL). $\{R = [-(CH_2)_3-NH_2]$; $R^1 = [CHO-(CH_2)_3-CHO]$; $R^2 = [=CH-(CH_2)_3-CH=]$

Fe_3O_4 previously obtained by MI, was added to a reaction mixture composed of 450ml ethyl alcohol, 450ml distilled water, 60ml ammonia (25%) and SF-Rb previously prepared. 5ml 3-Minotrioxisilan (300rpm, 600C) were added by dripping over this mixture. The obtaining reaction for the np-Rb, lasted for two hours. fter perfecting the coating reaction of Fe_3O_4 [8] and marking np

with Rb, the unfixed fluorochrome is removed by successive washing and centrifugation (3000rpm, $t = 5\text{min}$). The suspension ($\sim 1\text{-}2\%$) separated by unfixed Rb, was washed with distilled water until the pH value reached $7 \div 8$.

2.2 The obtaining of $(\text{ECH})_{n\beta}\text{-}\{\text{Fe}_3\text{O}_4\text{-n}[\text{SiO}_{1.5\gamma}\text{-(CH}_2)_3\text{(NH}_2)](\text{NH}_2)_{n\delta}(\text{Rb})_{np}\}\text{-(GL)}_{n\epsilon} \rightarrow (\text{ECH})_{n\beta}\text{-npa-(GL)}_{n\epsilon}$

Inserting a superficial layer of cross biochemical binding molecules, on the surface of the Fe_3O_4 nanoparticles covering layer, involves strict ordering and control of the obtaining procedures for the chemical reactions of activation [9]. Initially the S-ECH solution was obtained, composed of 0.3g NaOH, 2ml water, 20ml acetone and 0.5ml epiclorhidrina (ECH) [10]. This solution was agitated for twenty hours. The np-Rb obtained in the previous stage, are added to a volume of 600ml suspension, topped with distilled water. To this volume 7ml of glutaraldehyde were added and the pH was immediately adjusted to the value 11 with NaOH (1M).

The reaction was left to be perfected for 60 minutes (300rpm, 60°C). After perfecting the reaction, the suspension was washed as follows: (1) distilled water: twice (2) 200 ml of NaCl solution (0.2M) (3) distilled water: twice. Separations were made by centrifugation (3000rpm= v , $t=5\text{min}$), and the final pH of the suspension ($<1\%$) was brought to the value 7. The theoretical macromolecular chemical structure of the suspension obtained in this stage is of the $\text{Fe}_3\text{O}_4\text{-n}[\text{SiO}_{1.5\gamma}\text{-(CH}_2)_3\text{(NH}_2)](\text{NH}_2)_{n\delta}(\text{Rb})_{np}\}\text{-(GL)}_{n\epsilon}$ [npa-(GL)] type. The second stage of the chemical activation is initiated by the formation of a reaction mixture (600ml) consisting of npa-(GL) and S-ECH. The reaction is left to be perfected for an hour, and after perfecting the activation with activation ECH, the

obtained suspension was washed twice with distilled water.

The suspension bivalently activated with GL and ECH, obtained in this phase of chemical activation, has a theoretical chemical structure of the $(\text{ECH})_{n\beta}\text{-}\{\text{Fe}_3\text{O}_4\text{-n}[\text{SiO}_{1.5\gamma}\text{-(CH}_2)_3\text{(NH}_2)](\text{NH}_2)_{n\delta}\}\text{-(GL)}_{n\epsilon}$ [(ECH)-npa-(GL)] type [11] (Fig. 4).

2.3 (ECH)-npa-(GL) testing on ricin toxin (Tr)

Checking the effectiveness and efficiency of the biochemical fixation of (ECH)-npa-(GL) were performed by testing on ricin toxin (Tr) of bivalent enabled nanoparticles. For contrasting by confocal microscopy, of specific interaction regions between $\{(\text{ECH})\text{-npa-(GL)}\}$ and Tr, the Tr was marked with fluorescein isothiocyanate (FITC). The marking solution of Tr (S-Tr) consisted of 2ml castor, 1mg FITC and 20ml absolute ethylic alcohol. S-Tr was stirred for two hours (300rpm at room temperature). The biochemical fixation reaction consisted in the reaction 5ml S-Tr with 30ml (ECH)-npa-(GL) ($\sim 1\%$). The biochemical fixation reaction was left to be perfected for an hour (300rpm, 60°C). The obtained suspension was washed with distilled water, to remove traces of unfixed FITC in the molecular structure of Tr.

3. Results and discussions

Theoretical predictions that shape the biochemical fixing process state to obtain a complex macromolecular structure, such as $\text{Tr-}\{(\text{ECH})\text{-npa-(GL)}\}$ (Fig.5), resulted from the cross biochemical linkage process. To verify these assumptions the Leica TCS SP2 broadband multifoton spectral confocal microscope was used. The excitation was performed with an argon laser at $\lambda = 488\text{nm}$, in continuous wave. The VEGA II LMU transmission electronic microscope was used. This microscope has advanced microanalysis and chemical mapping possibilities. The microanalysis was performed using an X-ray spectrometer, model QUANTAX 400 with the following characteristics: (a) XFlash 4010 detector; (b) energy resolution: 125eV (Mn-K α); (c) Peltier cooling; (d) detection of the chemical elements contained between Be and U. The samples were deposited by dripping on a copper foil, and then dispersed with absolute ethylic alcohol. The experimental data resulted from the investigation of the $\{(\text{ECH})\text{-npa-(GL)}\}\text{-Tr}$ are shown in fig.7, fig.8, fig.9 (confocal microscopy – Leica TCS SP2), fig.10 and fig.11 (SEM - VEGA II LMU). The ricin toxin is a cytotoxic protein produced by the Ricinus communis plant, and is composed of

two glycoproteic chains: (a) A chain (RTA) - 32kDa; (b) B chain (RTB) - 34kDa [12]. The two glycoproteic chains are linked by a disulfide bridge. The crystalline cell of the castor belongs to the $P2_12_12_1$ group, having the following crystal parameters: $a=72.8\text{\AA}$, $b = 79.6\text{\AA}$ and $c = 114.7\text{\AA}$ [12].

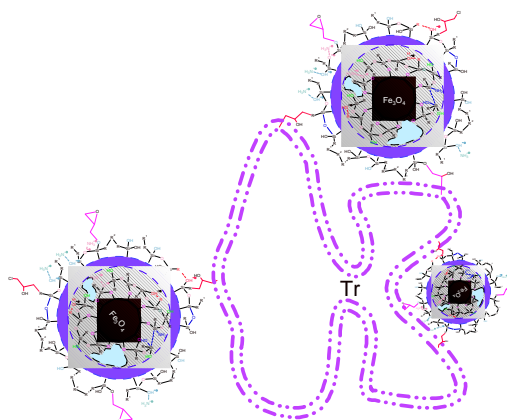


Fig.5 Theoretical mechanisms of the nondestructive biochemical fixation of $\{(ECH)-npa-(GL)\}$ on the surface of Tr

The B polypeptic chain is of lectinic nature, having the tendency of binding the galactose receptors or galactozamin N-acetyl on the surface of target cells, promoting endo-phagocytosis and toxin transfer to the Golgi apparatus [13]. Its length is of 70\AA and its approximated width is of 30\AA , being composed of two subdomains. Each subdomain has an approximately spherical shape with a diameter of 30\AA , able of fixing a disaccharides lactose molecule. The two subdomains fix galactose in the same way and have very similar topologies. The A chain only presents enzymatic activity when the B chain is released.

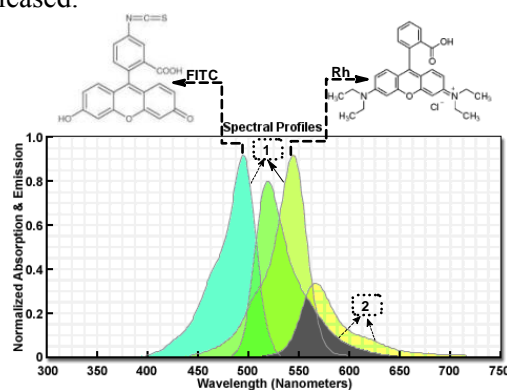


Fig. 6 Emission and adsorption spectral profiles of FITC and Rb
(www.olympusconfocal.com/java/dualprobes/index.html) 1- adsorption profiles; 2- emission profiles

The A chain has a high N-glycosidazical activity ($k_{cat}/K_m \sim 10^7 M^{-1} s^{-1}$, Endo and Tsurugi, 1988), helping the target citozol cells to adopt a temporary metastable state, then leave the Golgi apparatus (Argent et al., 2000). Once arrived in the interior of the cell, RTA acts as a proteins ribozomial inactivator, removing adenine bases from the RNA 28S ribosomes and preventing new protein synthesis (review - Lord et al., 2003). It has the shape of a globular protein, with the shape of an elongated disc with the length of 55\AA , width of 45\AA and thickness of 35\AA . The disulfide bridge between the two chains is formed between residue 259 of A chain and residue 4 of B chain.

FITC presents maximum adsorption at $\lambda = 495\text{nm}$ and a fluorescence emission spectrum that covers the $\sim 480\div 650\text{nm}$ spectral domain (maximum situated at $\lambda = 519\text{nm}$) (fig.6). The B rodamin shows maximum adsorption at $\lambda = 544\text{nm}$, and fluorescence emission spectrum spanning

over the $\sim 530\text{--}750\text{nm}$ spectral domain (maximum situated at $\lambda=566\text{nm}$) (fig.6). For $\lambda=488\text{nm}$ about 20% of the fundamental vibration levels of molecules of B rodamin are excited.

The analysis of fluorescence spectra (Fig. 9b, Fig. 9d, Fig. 9f) reveals a narrowing FITC emission spectrum by approximately 20nm. This change is due to the fundamental levels of electronic vibration of FITC molecules as a result of: (a) the establishment of stable chemical links between the $-\text{N}=\text{C}=\text{S}$ radical and the $-\text{NH}_2$ residue present in the Tr structure); (b) the changes occurring in the FITC energy configuration due to the local electronic effects.

The images and Rb fluorescence spectra may be difficult to notice in terms of intensity and quality of the acquired data. The intensities of the acquired images and fluorescence spectra are proportional to FITC and Rb concentrations found in the investigated region of interest (ROI). Given that the theoretical concentration of the (ECH)-npa-(GL) nanoparticles on the analyzed sample is much higher than the toxin macromolecule concentration, it is expected that the Rb spectrum and fluorescence images to be clearly defined and provide a higher density of fluorescence cores (relative to the density of the FITC cores unexcited by fluorescence) [14]. Fluorescence adsorption and emission spectra are related through the Jablonski diagram, which adds to the intensity of the fluorescence spectrum, a coefficient proportional to the excitation probability of the electronic vibration levels of the fluorophore (appropriate to the exciting wavelength being used). At $\lambda = 488\text{nm}$, the FITC and Rb extinction coefficients are of approximately 90% and respectively 16%. Even under these circumstances, one can satisfactorily notice both parameters [that define the morphology and topology Tr-{(ECH)-npa-(GL)}], and fluorescence spectra of (specific to FITC, Rb). The analytic interaction model of FITC with Tr, shown briefly in fig.5, is based on the following premises: (a) there are some limitation and orientation mechanisms of the number of (ECH)-npa-(GL) nanoparticles fixed on the Tr (b) the surface, molecular maps formed between (ECH)-npa-(GL) and Tr are characterized by regular homogeneous and isotropic patterns, throughout the biochemical fixation volume.

The morphotopology analysis (linear profiles shown in fig.8b, fig.8c, fig.8d, fig.11a, fig.11b) of the (ECH)-npa-(GL) and Tr dimensions (Tr $\sim 7\times 8\times 11.5\text{nm}^3$), indicates the fact that they are comparable. This represents one of the decisive factors that determine the number of activated nanoparticles attached to the Tr surface. The number of stable chemical cross-links established between the (ECH)-npa-(GL) and Tr (Fig. 5) is directly proportional to: (a) the (ECH)-npa-(GL) fixed on the toxin's surface; (b) the specific surface of the nanoparticles; (c) the (ECH) and (GL) density on the np surface. Obtaining (ECH)-npa-(GL) with optimal dimensions, in order to set a large number of cross biological and chemical fixation links, is an essential condition to be fulfilled in order to achieve: (a) transducing media with high biochemical fixing efficacy; (b) integrable transducing media in electronic detection systems and microsystems.

The acquired fluorescence images (Fig.7) are in concordance with the proposed model, observing that the distribution of the fixing mode of (ECH)-npa-(GL) around Tr, present the following morphostructural patterns: (a) (ECH)-npa-(GL) or Tr specific densities (per unit area / volume) are approximately equal; (b) areas bounded by the borders of interaction \leftrightarrow Tr (ECH)-npa-(GL) are approximately equal and regular.

From the analysis of the linear profiles acquired by means of SEM and confocal microscopy, and presented in Fig. 10a, Fig. 10c, Fig. 10d, Fig. 11a and Fig. 11b, one can estimate the average of the (ECH)-npa-(GL) diameters. We estimated that the (ECH)-npa-(GL) average diameter is of about 4-5nm and a proper dispersion (relative to the diameter) is less than one third of the diameter average ($\approx 1/3 \cdot 5 = 1.66 \rightarrow \delta d = d_{\text{mediu}} \pm 1.66\text{nm}$) [15]. The estimation of the nanoparticles' diameters was performed by comparative analysis of SEM and confocal linear profiles.

Analyzing the experimental data from fig.7 (a1, b1, c1, d1), fig.7 (a2, b2, c2, d2), fig.8a, fig.9a, fig.10(a, b, c, d), fig.11a, from the micromagnetic point of view [16], one can notice the formation of uniformly distributed magnetic domains in relation to the size. In the space between the magnetic domains, relatively evenly distributed (ECH)-npa-(GL) are positioned, as well as shallow surface densities which are much lower as compared to those in other areas. The approximate size of the magnetic domains is of $0.3\text{--}0.4\mu\text{m}$ in diameter and was estimated by comparative analysis of SEM and confocal linear profiles. The morphotopological analysis of the magnetic domains [performed by comparative analysis of: (a) the (ECH)-npa-(GL) density in regions of localized magnetic domains (fig.7c1, fig. 7c2); (b) the (ECH)-npa-(GL) dimensions] suggest a discoidal distribution of magnetic domains, being of a much lower height in relation to its length.

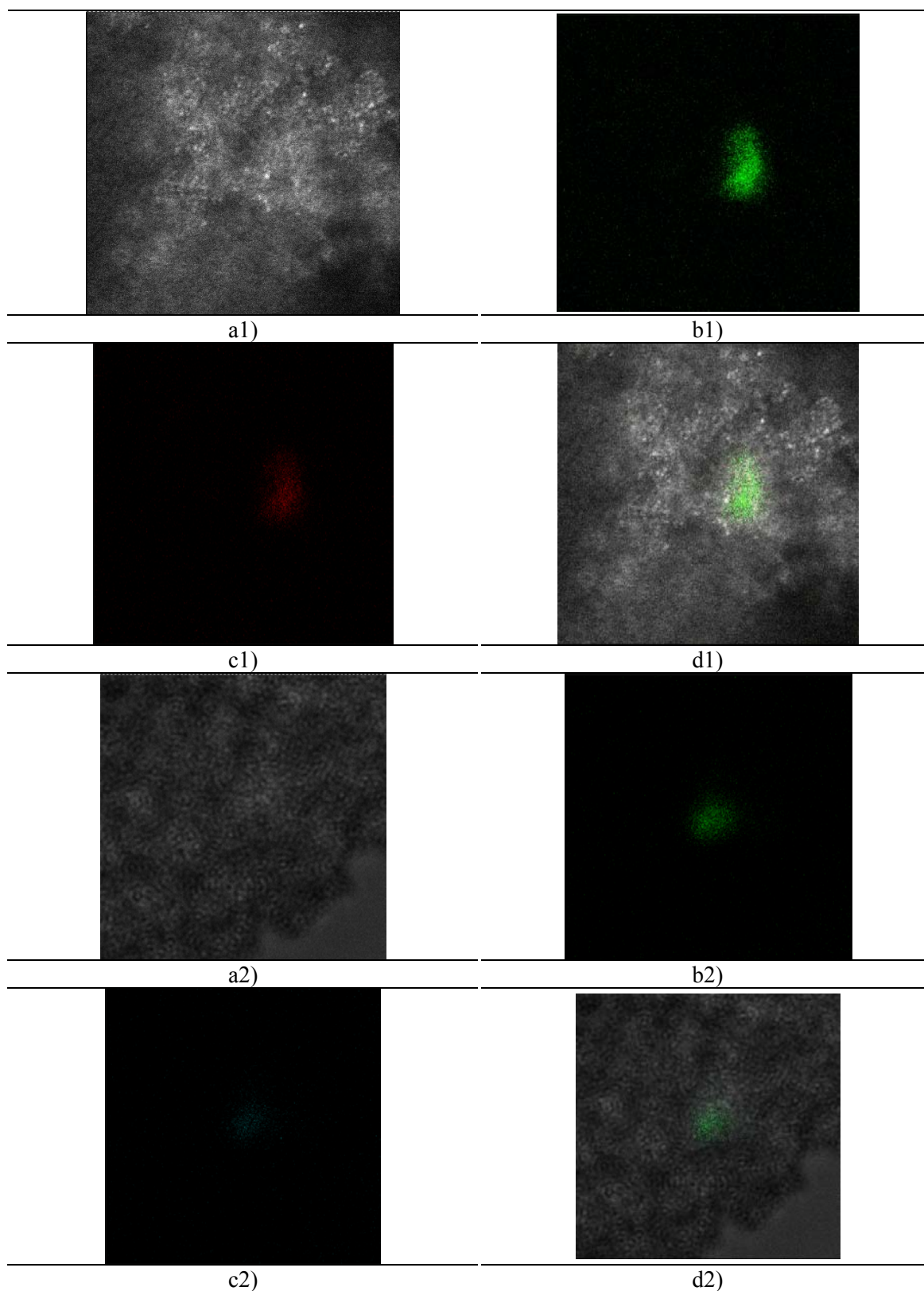


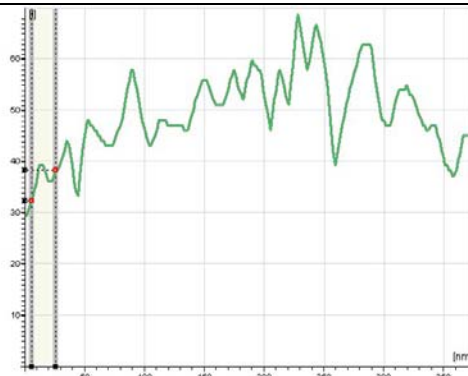
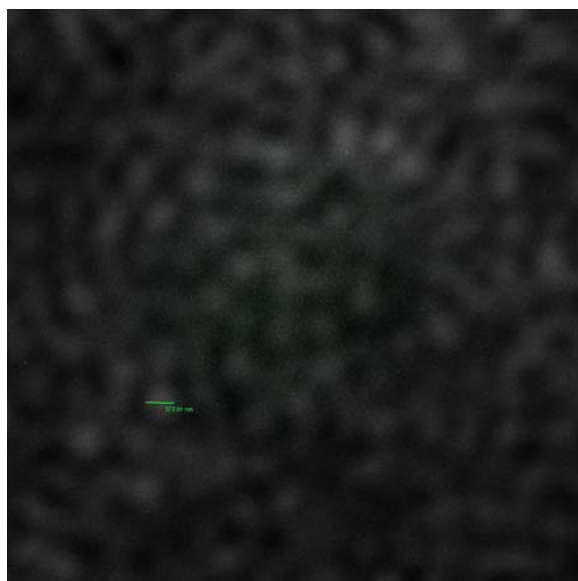
Fig.7 The acquired fluorescence images of the $(ECH)_{n\beta}\{-Fe_3O_4-n[SiO_{1.5}\gamma-(CH_2)_3(NH_2)](NH_2)_{n\delta}(Rb)_{n\rho}\}-(GL)_{n\epsilon}$ fixed on Tr. Each set (a1 , b1, c1, d1), (a2, b2, c2, d2) represents images acquired at the same point of the investigation sample, but the different mode of investigation (a1-image acquired by laser beam reflection on the sample, b1-image of a fluorescent FITC-Tr, c1-fluorescence image of $Fe_3O_4-n[SiO_{1.5}\gamma-(CH_2)_3(NH_2)](NH_2)_{n\delta}(Rb)_{n\rho}$, d1-superimposed image of the three separate images a1, b1 and c1). The experimental data set (a2, b2, c2, d2) is interpreted in the same manner.

Confocal experimental data show the Tr tendency to fix in the free space between the magnetic domains, where the (ECH)-npa-(GL) density is lower. Because testing was conducted under mechanical stirring conditions, (ECH)-npa-(GL) not showing magnetic flocculation phenomena, it results that during the fixation process of (ECH)-npa-(GL) on Tr rigid three-dimensional networks are formed. These networks are of various dimensions, either connected or separated. During the formation process of the magnetic domains, complex macromolecular networks of the $n\{(ECH)\text{-npa}\text{-}(GL)\}\text{-Tr}$ type are being formed (n = the degree of cross linkage between the $\{(ECH)\text{-npa}\text{-}(GL)\}\text{-Tr}$ that cannot defeat the local forces of magnetic viscosity [17]. The micromagnetic energy [18, 19] between the neighbouring (ECH)-npa-(GL), have a rapid attenuation in relation to the distance, because of the Fe_3O_4 nanoparticle size and the thickness of the $n[\text{SiO}_{1.5\gamma}\text{-(CH}_2)_3\text{(NH}_2)]\text{(NH}_2)_{n\delta}$ covering layer. There are cases (fig.7b1, fig.7b2) in which $\{(ECH)\text{-npa}\text{-}(GL)\}\text{-Tr}$ macrocomplexes are included in the interior of the formed magnetic fields.

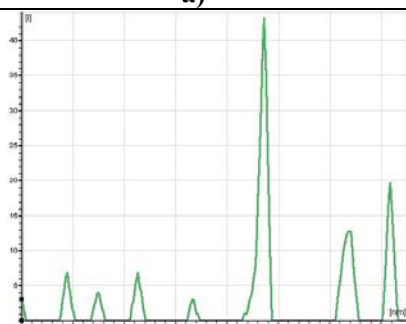
This fact can be explained admitting the fact that n has very small values (eg.: the surface of a Tr molecule is saturated with (ECH)-npa-(GL) \rightarrow the complex does not set any other biochemical cross-links with the neighboring macromolecular structures). The FITC fluorescence spectra (fig.9b,fig.9d), indicates the emergence of distinct picks over the $\sim 510\text{-}524\text{nm}$, $\sim 572\text{-}581\text{nm}$ spectral domains and the approximate wave lengths: 534, 542 and 551nm. These picks change the emission pattern and become more pronounced with the increasing of: (a) the density of $\{(ECH)\text{-}\{npa\text{-Rb}\}\text{-}(GL)\}\text{-Tr}$, per unit of analyzed area; (b) the volume of the magnetic domain formed by $\{(ECH)\text{-}\{npa\text{-Rb}\}\text{-}(GL)\}\text{-Tr}$ (fig.9b, fig.9d).

taking these considerations into account, it is very likely that these picks are due to the contribution of the Rb generated fluorescence processes to the FITC fluorescence emission (in the overlap region) [20]. In fig.9b the FITC fluorescence spectrum can be clearly observed, as compared to that of the Rb, which contains a series of negative and weak intensity picks. There is a high probability that during the fluorochromic marking of the npa with Rb, ion clusters $\equiv\text{N}^+\text{Cl}^-$ and $-\text{CO}^-$ radicals should establish covalent chemical bonds, or of electrostatic nature, with the ($-\text{OH}$, $\equiv\text{Si-O-Si}\equiv$, etc.) hydrolysable bonds of the $n[\text{SiO}_{1.5\gamma}\text{-(CH}_2)_3\text{(NH}_2)]\text{(NH}_2)_{n\delta}$. In this case, as a result of the modifications in the fundamental levels of the Rb vibration energy, a significant change of the pattern of the fluorescence emission spectrum results. As a result of the increasing density, per unit volume $\{(ECH)\text{-}\{npa\text{-Rb}\}\text{-}(GL)\}\text{-Tr}$, the npa-Rb amount contained increases proportionately, resulting in a more pronounced influence effect of the FITC fluorescence spectrum. These observations were constantly confirmed during the performed analysis by means of confocal microscopy, both in the (relevant) acquired experimental data, and in the case of the optimization ones of the optoelectronic acquisitions.

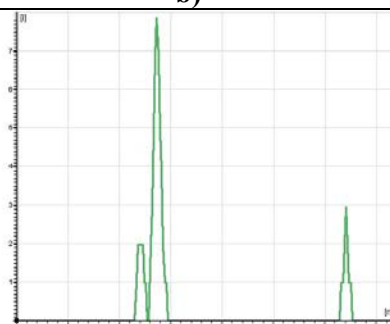
The assumption of overlapping the FITC and Rb fluorescence emission spectra satisfactorily explain the fluorescence emission patterns in the case of FITC (different from the ones established in physico-chemical predefined conditions).



ROI→ROI 1 (reflexion image)	Standard Deviation→8.05
Length→373.81 nm	I (x1)→ 33.00 (6.13 nm)
Mean Amplitude→50.28	I (x2) →39.00 (26.04 nm)
Max. Amplitude→70.00	Min. Amplitude→30.00 nm)
Average Deviation→6.51	dl→6.00 dx→19.92 nm

a)

ROI→ROI 1 (Tr-FITC)	Min. Amplitude→0.00
Length→373.81 nm	Average Deviation→3.54
Mean Amplitude→2.45	Standard Deviation→6.21
Max. Amplitude→44.00	

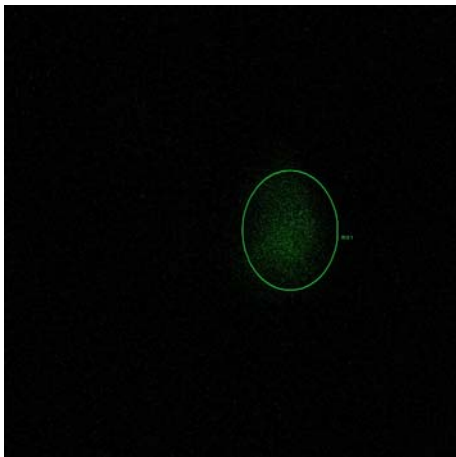
c)**b)**

ROI→ROI 1 ((ECH)-npa-(GL)-Rb)	Max. Amplitude→8.00
Length→373.81 nm	Min. Amplitude→0.00
Mean Amplitude→0.27	Average Deviation→0.49
	Standard Deviation→1.05

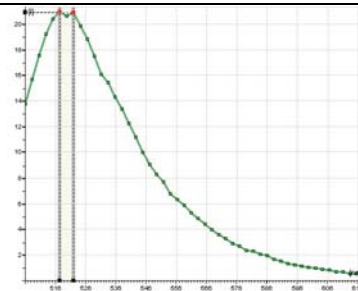
d)

Fig.8 Aquired linear profiles of the investigated samples: a) image acquired by reflecting; b) linear profile of FITC-Tr; c) linear profile acquired on the detection channel (ECH)-{npa-Rb}-(GL)

Analyzing the patterns of interaction between the (ECH)-{npa-Rb}-(GL) and the Tr-FITC (fig.7, fig.8, fig.9), a precise location is observed and significant amounts of Tr - FITC on the (ECH)-{npa-Rb}-(GL) surface. Some microregions exist on the fluorescence images which reveal the formation of rigid three-dimensional networks of the Tr↔(ECH)-{npa-Rb}-(GL) type (previously treated).

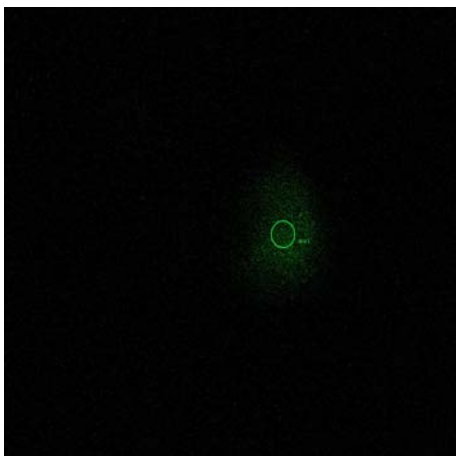


a)

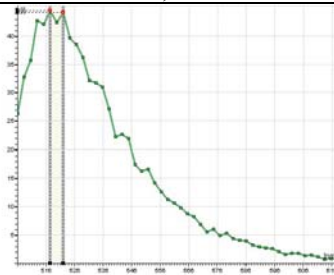


ROI→ROI 1 (FITC)	Pos. Min.
Pixel(ROI) →45530.00	Ampl→615.76 nm
Area→283.55 μm^2	Average
Length→618.00 nm	Deviation→6.41
Mean	Standard
Amplitude→8.04	Deviation→7.30
Max.	I (la1)→ 21.35 (517.43 nm)
Amplitude→21.35	I (la2) →21.32 (522.00 nm)
Pos. Max. Ampl.	dI→0.03
→517.20 nm	dla→4.57 nm
Min. Amplitude→0.49	

b)

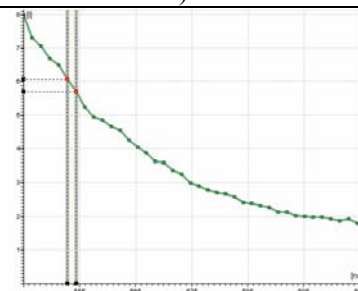
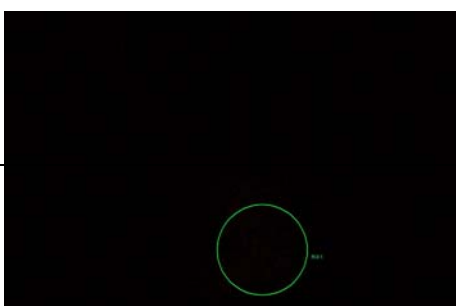


c)



ROI→ROI 1 (FITC)	Pos. Min.
Pixel(ROI) →2458.00	Ampl→611.28 nm
Area→15.31 μm^2	Average
Length→618.00 nm	Deviation→13.30
Mean	Standard
Amplitude→16.40	Deviation→15.25
Max.	I (la1)→ 45.35 (517.43 nm)
Amplitude→45.35	I (la2) →45.07 (522.00 nm)
Pos. Max. Ampl.	dI→0.28
→517.20 nm	dla→4.57 nm
Min. Amplitude→0.74	

d)



	Pos. Min.
ROI→ROI 1 (Rb)	Ampl→604.48 nm
Pixel(ROI) →32580.00	Average
Area→16.28 μm^2	Deviation→1.49
Length→606.00 nm	Standard
Mean	Deviation→1.81
Amplitude→3.70	I (Ia1)→ 6.17 (552.82
Max. Amplitude→8.13 nm)	
Pos. Max. Ampl.	I (Ia2) →5.80 (554.38
→545.00 nm	nm)
Min. Amplitude→1.82	dI→0.37
	dIa→1.56 nm
e)	f)

Fig.9 FITC fluorescence images [(a), (c)] and Tb (e); the FITC fluorescence spectra [(b), (d)] and Tb (f)

Assuming a structural formula of the $n[(\text{ECH})\text{-}\{\text{npa-Rb}\}\text{-(GL)}]\text{-}m[\text{Tr-FITC}]$ type (m, n are multiple cross biochemical binding coefficients), for the rigid three-dimensional networks being formed, it results that the interaction time between the activated nanoparticles and the ricin is a very short one.

As a consequence of the short biochemical fixing times, the contact microregions between $n[(\text{ECH})\text{-}\{\text{npa-Rb}\}\text{-(GL)}]$ and $m[\text{Tr-FITC}]$ are practically „frozen” in the initial contact state, due to the differences in solubility and difuzivity which exist between $(\text{ECH})\text{-}\{\text{npa-Rb}\}\text{-(GL)}$ and Tr-FITC .

The combined interpretation of the data acquired by means of the SEM and EDX microanalysis (fig.10), supports the experimental data acquired by means of confocal microscopy, and the assumptions discussed earlier, regarding the mechanisms invoked during the cross biochemical fixation process. The acquisition process of the chemical distribution patterns (EDX microanalysis) was stopped after a certain period of time, relevant for highlighting the distribution of chemical elements which are consisted in the NPA and Tr structure. The extension of the acquisition period of the distribution patterns would have lead to the impossibility of discriminating between two neighbouring fields [15], composed of distinct chemical elements, whose physical dimension is smaller than that of the pixelizing rezolution. It it interesting to observe (fig.10a, fig.10b, fig.10c) that nitrogen presents a remarkable uniformity of distribution on the entire scanned surface (in relation to Fe, Si, O), faithfully copying the predicted theoretical patterns for npa.

Is is most likely that the patterns situated at the borders between the npa and in which a significant quantity of nitrogen is distributed correspond to the Tr macromolecules. In its turn, the Tr surface is completely saturated with npa, which are chemically or magnetically unflocculated, and fixed rigidly on the toxin's surface. The patterns corresponding to the overlapping Fe, Si, O, are nanoregions of the npa and do not contain fixed Tr macromolecules.

4. Conclusions

In the present paper paramagnetic nanoparticles were obtained by the reverse micelle technique, polyvalently activated from the biochemical point of view. The general chemical structure of these nanoparticle class is of the following type $(\text{ECH})_{n\beta}\text{-}\{\text{Fe}_3\text{O}_4\text{-}n[\text{SiO}_{1.5\gamma}\text{-(CH}_2)_3(\text{NH}_2)](\text{NH}_2)_{n\delta}(\text{Rb})_{n\rho}\}\text{-(GL)}_{n\epsilon}$ $\{\text{npa}\}$ $\{\beta, \epsilon$ - biochemical activation coefficients by epichlorhidrine, glutaraldehyde respectively \rightarrow amount of aminated groups supplementary inserted in the covering layer structure, in relation to the theoretical amount of $n[\text{SiO}_{1.5\gamma}\text{-(CH}_2)_3(\text{NH}_2)]$; ρ - marking coefficient of the covering layer with rhodamine B \rightarrow the amount of Rb fixed in the covering polymeric structure; γ - hydrolysis coefficient of the -OH groups belonging to $\text{Si}(\text{OH})_3\text{-(CH}_2)_3(\text{NH}_2)\}$.

The obtained npa were tested on ricin toxin in order to determine: (a) the biochemical fixation efficiency and effectiveness (b) the biochemical fixation mechanisms (c) the specific

morphotopology for the fixation process (d) the opportunity of using these nanoparticles as host and transducer media, integrated automated sensors and biochemical microsensors.

The samples were investigated by means of confocal microscopy, SEM and EDX microanalysis, in order to determine comparatively the fixation mechanisms, the biochemical fixation efficiency and effectiveness. As a result of the investigations it was found that the npa shows a particular affinity in relation to ricin, the fixing of this toxin having been performed in a nondestructive manner, with high efficiency and effectiveness.

Also, as a result of the microscopic investigations it was found that npa shows a small dispersion in relation to its dimensions, and a high diffusion coefficient. As a result of the findings in the present paper, it can be concluded that the npa can form uniform nanometric films, can successfully form interfaces with the surfaces (a), thin metallic layers, (b) thin oxide layers – SiO₂, ZnO₂, TiO₂, ferrites, alloys, etc. Due to the npa's high biochemical fixing effectiveness and efficiency, the interfaces implemented by these nanoparticles with the detectors media fulfill the signal specific biochemical amplifiers function, favouring the detection, the identification and quantification of analytes that are of interest (eg, toxins, microorganisms, organic metabolites, etc.). In this case, the most utilized biochemical stimuli are the electromagnetic radiations from the UV spectrum (laser, diode, LED, gas plasma, etc.).

This experimental data was feasible thanks to 31-001/2007, 81-002/2007 and 32-165/2008 projects, inside PNI research program

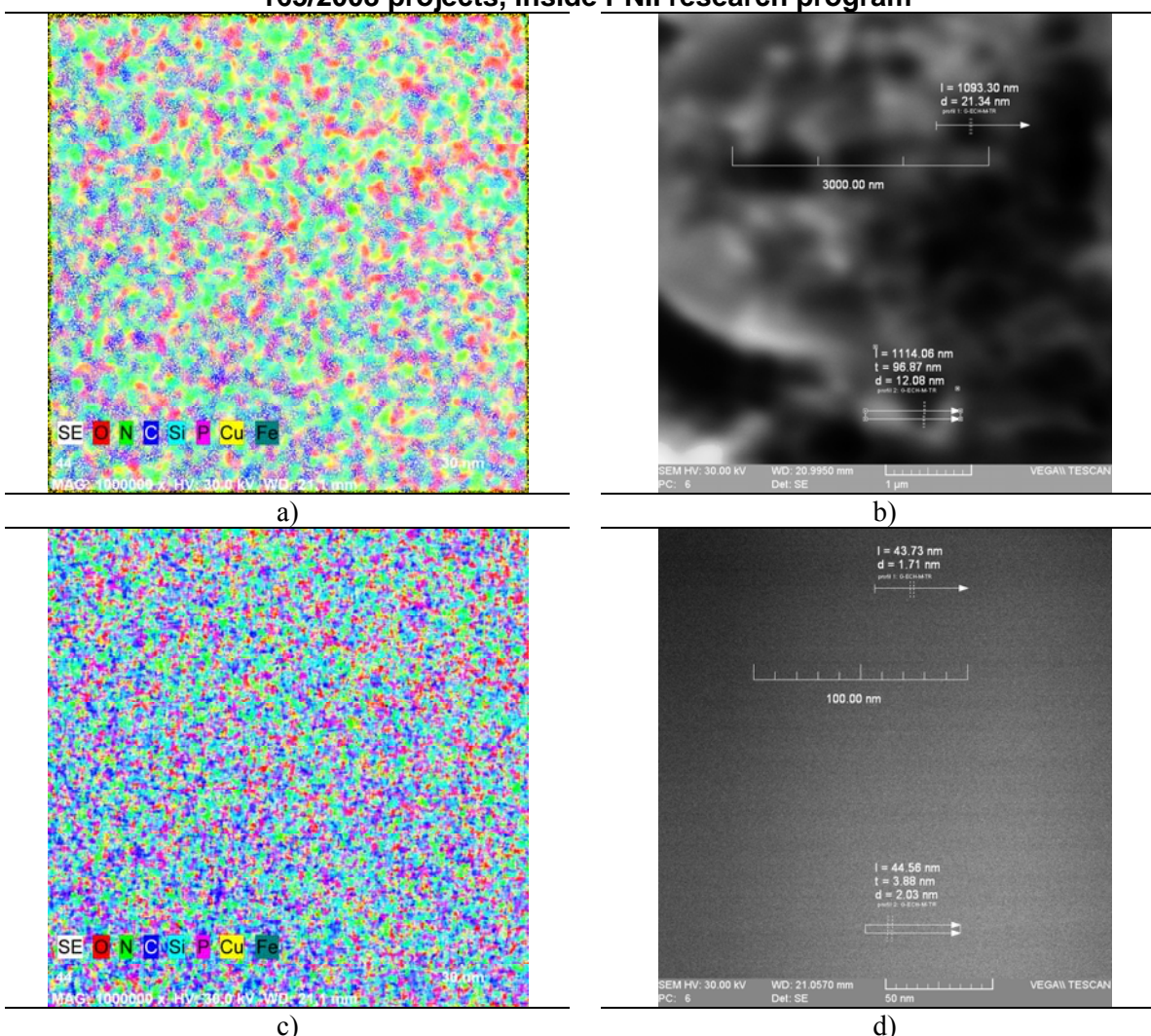
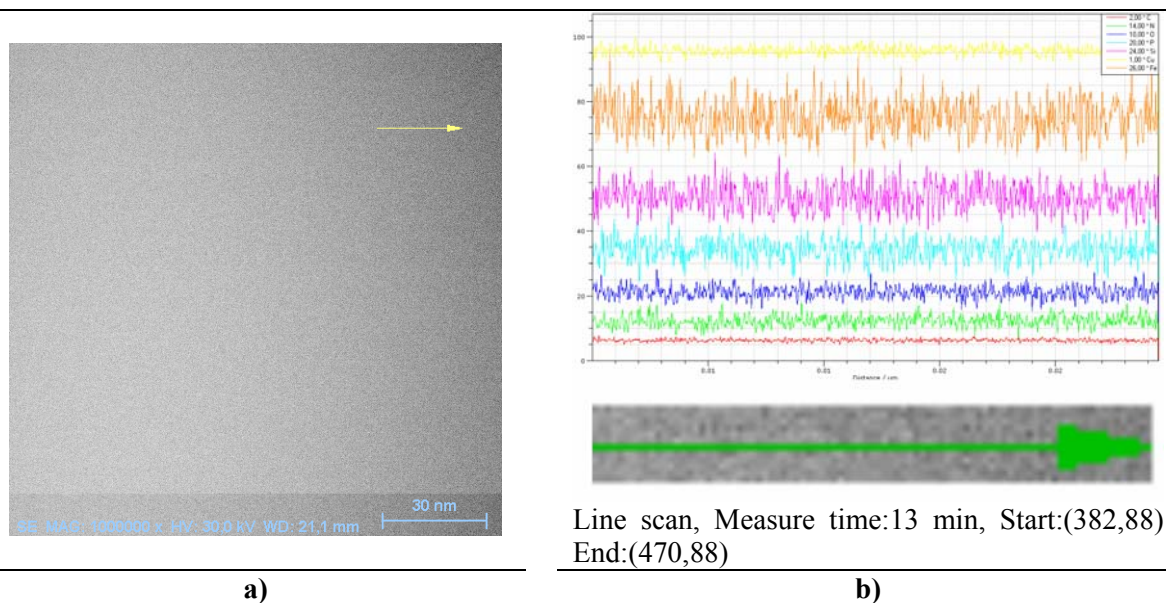


Fig.10 SEM and EDX microanalysis images of the samples (ECH)-{npa-Rb}-(GL)-Tr: a), c) SEM+microanalysis combined images b) separated chemical distribution of the wanted chemical elements d) SEM image



a) **b)**
 Fig.11 Linear profile microanalysis: a) SEM image of the sample and linear profile on which the microanalysis is applied b) experimental acquisition data on the imposed profile

References

- [1] J. Fraden, Handbook of Modern Sensors: Physics, Designs, and Applications, **3rd ed.**, Springer, Berlin, Heidelberg, New York (2005).
- [2] G. van der Horn, J. H. Huijsing, Integrated Smart Sensors: Design and Calibration, **1st ed.** (1997).
- [3] I. J. B. Visniac, Electromechanical Sensors And Actuators, Springer-Verlag New York (2007).
- [4] P. Z. Iordache, V. Şomoghi, N. Petrea, R. Petre, B. Dionezie, V. Ordeanu, A. Hotăranu, L. Mutihac, J. Optoelectron. Adv. M., **11**, 5, 736 – 743, (2009).
- [5] E. L. Duarte, R. Itri, E. Jr. Lima, M. S. Baptista, T. S. Berquó, G. F. Goya, Nanotechnology, **17**, 5549–5555 (2006).
- [6] P. C. Hiemenz, R. Rajagopalan, Principles of colloid and surface chemistry, **3rd ed.**- rev. and expanded, Marcel Dekker, New York (1997).
- [7] F. A. Tourinho, R. Franck and R. Massart, J. Mater. Sci. **25**, 3249 (1990).
- [8] P. Z. Iordache, V. Şomoghi, I. Savu, N. Petrea, G. Mitru, R. Petre, B. Dionezie, V. Ordeanu, L. Kim, L. Mutihac, J. Optoelectron. Adv. M., **2**, 8, 491 – 497 (2008).
- [9] Z. H. Xu, Q. X. Liu, J. A. Finch, *Applied Surface Science*, **120**, 3-4, 269-278 (1997).
- [10] H. W. Gu, Z. M. Yang, J. H. Gao, C. K. Chang, B. Xu, *J Am Chem Soc*, **127**, 1, 34-35 (2005).
- [11] A. del Campo, T. Sen, J. P. Lellouche, I. J. Bruce, J. Magn. Magn. Mater., **293**, 1, 2005.
- [12] W. Montfort, J. E. Villafranca, A. F. Monzingol, S. R. Ernst, B. Katzin, E. Rutenber, N. H. Xuong, R. Hamlin, J. D. Robertus, J. Biol. Chem, **262**, 11, 5398-5403 (1987).
- [13] J. M. Guyot, M. Helmy, S. L. Frasca, D. Pignol, G. Piéroni, B. Beaumelle, J. Biol. Chem, **278**, 19, 17006-17011 (2003).
- [14] C. J. R. Sheppard, A. Choudhury, Opt. Acta., **24**, 1051-1073 (1977).
- [15] E. H. K. Stelzer, J. Microsc. (Oxf), **189**, 15-24 (1997).
- [16] R. Skomski, J. Zhou, Advanced Magnetic Nanostructures, Springer, **ch.3** (2006).
- [17] E. Lima Jr., A. L. Brandl, A. D. Arelaro, G. F. Goya, J. Appl. Phys., **99** (2006).
- [18] W. F. Brown, Micromagnetics, Wiley, New York (1963).
- [19] A. Aharoni, Introduction to the Theory of Ferromagnetism, University Press, Oxford (1996).
- [20] H. H. Hopkins, Proc. Phys. Soc., **55**, 116-120 (1943).